Reconfigurable Geometrical Phase Spatial Light Modulator Using Short-Pitch Ferroelectric Liquid Crystals

Abhishek Srivastava (✉ eeabhishek@ust.hk)
Hong Kong University of Science and Technology

Zhi-Bo SUN
State Key Laboratory of Advanced Displays and Optoelectronics Technologies, Hong Kong University of Science and Technology

Zheng-Nan YUAN
State Key Laboratory of Advanced Displays and Optoelectronics Technologies, Hong Kong University of Science and Technology

Vigneshwaran Swaminathan
State Key Laboratory of Advanced Displays and Optoelectronics Technologies, Hong Kong University of Science and Technology

Valerii Vashchenko
State Key Laboratory of Advanced Displays and Optoelectronics Technologies, Hong Kong University of Science and Technology

Olena Vashchenko
State Key Laboratory of Advanced Displays and Optoelectronics Technologies, Hong Kong University of Science and Technology

Alex Yuk Lung Cheung
State Key Laboratory of Advanced Displays and Optoelectronics Technologies, Hong Kong University of Science and Technology

Lei LU
State Key Laboratory of Advanced Displays and Optoelectronics Technologies, Hong Kong University of Science and Technology

Hoi-Sing Kwok
The Hong Kong University of Science and Technology

Article

Keywords: Phase modulation, Deformed helix ferroelectric liquid crystal, Geometrical phase, Adaptive optics, Beam steering, Hologram, LiDAR

Posted Date: February 27th, 2023

DOI: https://doi.org/10.21203/rs.3.rs-2612551/v1

Abstract

This article shows a fast continuous 2π geometrical phase modulator based on the dynamic optical axis rotation of the short-pitch Ferroelectric Liquid Crystal (FLC). A continuous multi-level (8-bit) phase modulation, fast switching time (< 250 µs at 2 kHz), low operating voltage (< 7 V), and high diffraction efficiency (> 77%) is achieved using defect-free Deformed Helix Ferroelectric Liquid Crystal (DHFLC) for the first time. We showed a minimum feature size of 1 µm without fringe field effect (FFE). We also developed a new FLC with a cone angle of ~85˚ and a way to provide compensated half-wave condition (HW) during the entire electro-optical operational range. As a result, we achieve both spatial and time modulation with high frequency (1/3 μm^{-1} and 4 kHz, respectively), which can be used in applications such as a real-time hologram and dynamic beam steering in Light Ranging and Detector (LiDAR).

Introduction

Recently, Spatial Light Modulators (SLMs) with high modulation bandwidth in both spatial and time domains received great interest. Especially SLMs with small pixel size and continuous 2π phase modulation are in great demand for applications such as Light Detection and Ranging (LiDAR), holographic display, AR/VR, optical tweezers, correction in digital photo-lithography, wave-front correctors, 3D printing, and correlator in free space optical calculation, communications, and many more[1-10]. Such SLMs can also be used in the blocks of optical information processors, high-resolution microscopy, and display applications[11]. For instance, it can be used in Adaptive Optics (AO), which is paving the way for high-resolution microscopy, and aberration correction in biomedical imaging including the biological tissue specimens, cell structure, and pico-scale devices[14].

The SLMs can be categorized into two types. First, micro-mirrors based devices that include Micro-electro Mechanical systems (MEMS) and bimorph deformable mirrors[16]. These are generally employed for binary modulation offering high-frequency operations (f < 20 kHz) with fixed amplitude and phase by addressing the light reflection. Digital Micromirror Devices (DMD) SLMs are effective for direct-laser-projection (DLP), 3D printing and aberrations correction in two-photon imaging[19]. However, the non-solid structure and binary modulation are serious barriers for applications that require frame rate above kHz, multi-phase-level, and reconfigurable phase modulators. On the other hand, there are modulators based on Liquid Crystals (LC). These modulators are tuneable with highly flexible patterns[20-22]. LC SLMs use LC's ability to respond to external stimuli, mostly applied electric fields. In contrast to the DMD SLMs, the LC-based SLMs have advantages in generating complex phase patterns. Moreover, it can potentially find application in multi-photon microscope that requires a correction element in the illumination path[12]. Besides, the LC SLMs can readily be employed in two-photon fluorescence microscopes since phase modulation is necessary for the laser beam, not the fluorescence output[13,23-25]. Apart from AO, phase modulation has been extensively explored for hologram and beam steering. Recently, the Polymer-stabilized Blue Phase Liquid Crystals (PSBPLC) and standing helix Cholesteric Liquid Crystals (CLC) based SLMs were reported for display applications[26,27].

Liquid crystal on silicon (LCoS) technology can be utilized for developing SLMs based on Nematic LC (NLC) or FLC. However, the NLCs can only achieve low-frequency phase modulations due to its slow switching time, typically < 180 Hz[28]. The LCoS using Surface Stabilized Ferroelectric Liquid Crystal (SSFLCoS) usually provides fast (~10 kHz)[29,30], with only binary phase modulation[31-32,33].

The Deformed Helix Ferroelectric Liquid Crystal (DHFLC) with sub-wavelength helix pitch can provide continuous amplitude modulation without fringe field effect (FFE.)[34,35]. The DHFLC, on applying the electric fields, shows a continuous change of effective birefringence and the optical axis, resulting in analog grayscale [36]. However, there are certain limitations, such as loss of light due to the imperfect alignment in the DHFLC that limits the efficiency and contrast ratio in these devices[36]. Additionally, the effective birefringence and effective optical axis change simultaneously[32,35]. The variation of the retardation limits the multi-phase level and phase modulation depth. Furthermore, the phase modulation depth depends on the rotation cone of the DHFLC optical axis, and the required cone angle of FLC should be close to 90°, which usually increases the rotational viscosity and limits the response time of the FLC[31].

Bottlenecks

The minimum pixel size, resolution, FFE., response time of LC, and the driving voltages are the critical attributes of a high-performing LCoS. Currently, LCoS occupies the market of the most competitive phase modulators with 2π phase modulation range such as Wavelength Selective Switch (WSS) and near-eye holographic displays. Due to growing demand in high-resolution imaging and photonic devices, people are aiming to archive LCoS pixel size ~ 1 μm without any artifact. However, reducing the pixel size of LCoS is challenging for NLC due to strong FFE. (crosstalk)[34]. A relatively large pixel size results in low diffraction efficiency, a small deflection angle, and a hologram with a limited viewing zone.

The FFE. is a common issue in devices with an electrode array that has voltage distribution in 1D, 2D, or 3D patterns, which is also referred to as the cross-talk effect between neighboring pixels. It becomes a serious issue for devices using a vertical electric field as a driving force, such as twisted nematic LC, pi-cell LC (O.C.B.), and nonlinear optical materials, especially when the thickness of the LC is comparable to the pixel size. To evaluate the severity of the FFE. in modern high-resolution devices, a common Electrical Controlled Birefringence (ECB.) LC cell (cell gap = 4.3 μm) filled with nematic MLC2144 (Merck & Co. Inc)[39] condition is simulated using the LCD master simulation software, see Fig. 1a. Ideally, the phase depth should reach 2π in the absence of FFE. and should not have disclination lines, but these two factors are inevitable for NLCs[34]. Specifically when the pixel size is 3.54 μm with 0.2 μm electrode gaps for 4K LCoS devices. Here two kinds of FFE. are considered[38]. Firstly, the FFE. induced by the horizontal electric field, results in the disclination line. Secondly, the FFE. induced by the vertical electric field , which results in the cross-talk between pixels. In Fig. 1a, on applying different voltages on neighbouring pixels, the phase modulation depth drops by 30% and serious disclination lines show up at driving voltage 0.79 V. On comparing it with the ideal phase modulation profile on each electrode, we found a clear mismatch

and disclination lines. In spite of several efforts, the FFE. and slow response times remains the two main issues for modern NLC based SLMs. These limitation results in, insufficient spatial frequency, deflection angle (< 2˚), efficiency and refresh rate stopping NLS based LCoS towards a lots of applications such as hologram, WSSs, and LiDARs[40].

In 2020, our group showed that the DHFLC based spatial light modulators are inherently immune to FFE. [34]. The DHFLC shows a clear electrode edge without any noticeable FFE. or disclination lines, whereas these effects are serious in NLCs[34]. The POM. images of NLCs and DHFLCs are shown in Fig. 1b. Fig. 1c and d depicts the configuration of FLC cell, the FFE. is primarily absent due to the coupling between the electric field and spontaneous polarization (). The in-plane direction of alongs the FLC helix axis, the E_x does not couple with , and therefore, FLC molecules do not respond to the . Conversely, the electric field projections are perpendicular to the helix axis couple with FLC molecules. However, unlike the ECB. in NLC and Kerr effect in vertical aligned deformed helix ferroelectric liquid crystal, planar aligned FLC shows limited performance in phase modulation because of the hysteresis and limited modulation ability. In 2022, Nabadda et al proposed an optimized binary phase modulation using the SSFLC mode. Optimizations related to the FLC materials and optics are still on going[41]. Kotova, S. P. et al proposed a continuous phase modulation by using DHFLC while the cell gap is around 50 μm for visible light, for which the alignment quality and FFE. should be discussed and optimized[32].

In this article, a fast continuous 2π geometrical phase modulator on the basis of dynamic rotation of the short-pitch Ferroelectric Liquid Crystal (FLC) is proposed. A continuous multi-level (8 bit) phase modulation with 1.9π phase modulation depth, fast switching time (<250 μs), low operating voltage (< 7 V) and high diffraction efficiency (> 77%) is achieved based on defect-free Deformed Helix Ferroelectric Liquid Crystal (DHFLC) for the first time while the minimum distinguishable feature size is 1 μm, without FFE. We also discussed the unwinding process of the helix, linear working region of DHFLC for pure phase modulation, using rotation of the effective optical axis, and non-linear phase modulation region using the change of the effective birefringence, are shown as the limitation and introduction of the dynamic unwinding of DHFLC. We synthesized a new series of FLC material with fast response and cone ~ 85˚ for short pitch DHFLC. Later, we designed a compensation film to enlarge the phase modulation depth in and beyond the material aspect of DHFLC. We also illustrated that DHFLC is a promising candidate for LiDAR, real-time holograms and other spatial light modulator applications requiring fast response and super high pixel density.

Material Design

To design a suitable short pitch FLC, we used the guest host approach, wherein the achiral host is mixed with one or multiple chiral guest molecules. The chiral components were synthesized using the similar approach described in Ref [42]. The details of FLC materials synthesis are given in Supplementary Materials 1.1-1.3.

General requirements of the high-performing DHF. materials for the electro-optical application includes short helix-pitch () (*i*) to avoid Bragg diffraction of light, at any angle of incident, must be <125-130 nm; (ii) and maintain high elastic energy during the whole operational range[43]. The induced helix-pitch of FLC, based on guest host approach, depends on concentration () of the chiral component (CC) and its helical twisting power (HTP.), which can be written as $p^{-1} = H.T.P. \times c \times ee$, where *ee* is enantiomeric excess of CC.

Typically, the viscosity of FLC increases with the concentration of CC. Thus, a chiral compound with high H.T.P. is required that can achieve short helix-pitch at relatively lower content of CC in achiral host. To achieve a maximum phase modulation depth, tilt angle should be 45°. However, a slightly small , even ~ 40°, still provides reasonably high phase modulation range and diffraction efficiency. Furthermore, to meet the higher resolution SLM. limitations on the driving voltage, the spontaneous polarization () of the FLC should be high, which adds additional constraints on the concentration of the CC.

We started from the mixture FLC 587[42] and considered as our reference material. The FLC 587 show FFE-free phase and amplitude modulation[34]. This mixture is composed of binary biphenylpyrimidine host (BPP-6587) and 24 mol.% of CC FOTDA-6, see Table 1. Since BPP-6587 melts at 36°C, to have a non-crystallized FLC mixtures at room temperature, we compose new 6-component host, BPP-73, which melts at 21°C. We suppose that an additional dipole to the structure of the CC can enforce the inter-molecular interaction with host molecules and thereby improve H.T.P. and P.S., we synthesised o-diflouro analog of **FODTA**, compound **DFT-TFA-6**. Indeed, **DFT-TFA-6** shows increased H.T.P. (by ~10%), whereas *P.S.* value remains almost unchanged, *c.f.* 9074 with 9075. However, unexpectedly new CC induced higher tilt angle (~ 42.5° at room temperature). Further variation of chemical structure of FODTA, namely exchange terminal of benzene rings with pyridine ones, passing to PDN-TFA-6 CC, resulted in further enhancement of the CC performance: H.T.P., and especially , see Table 2. Apparently, the pyridine rings increase the inter-molecular coupling not only due to dipole-dipole interaction, but being of the basic nature, also by specific interaction with surrounding molecules.

Results

The helix pitch of our FLC materials, at room temperature, is in the range of 90–125 nm. Though the pitch is sufficiently smaller than the visible wavelength to avoid optical artifacts due to Bragg diffraction, we need to understand the unwinding mechanism of pitch under the applied electric field. Thus, to study the helix-pitch (p) of DHFLC during the whole unwinding process, a cell filled with DHFLC with thick copper (Cu) electrode walls (25 μm in height-derived from the electrophoresis method) is placed between a wide spectrum light source and the spectrometer, see Fig. 2a. Initially the measurement was performed at the room temperature (where p = ~120 nm) as a function of applied electric field, but no peak observed in the visible spectrum suggesting that the whole unwinding process happens well below the visible range hence no artifacts due to Bragg diffraction shows up. However, in order to observe and understand the unwinding process the sample was heated to 60°C, where the helix-pitch is slightly unwounded (due to temperature) and show the Bragg selective reflection at λ = 450 nm in the absence of the electric field (dark blue color show up in Fig. 2a( )). By gradually increasing the applied electric field between the 2

copper walls, the DHFLC starts to unwind, leading to the peak shift of the Bragg reflection. Firstly, the peak just show a red shift, then it separates into multiple peaks with wider spectrum width. With large enough electric field, the reflected peak totally disappears within the whole spectral range, confirming the complete helix unwinding. Because the elastic energy of DHFLC is much greater than the electrical potential energy, the translation of the reflected peak at small electric field is shown as shifting with single selective reflection. In other words, the helix-pitch undergoes a deformation, leading to the optical axis rotation and phase variation. With the change of helix-pitch during gradually increasing applied E, the periodical helix remains unchanged until to a certain threshold electric field, which is described as linear region ($\delta\left(\Delta n\right) \approx 0$) in Fig. 3. After that, it steps into the broken-helix region where $\delta\left(\Delta n\right) \neq 0$, leading to several periodical structures that becomes the superposition of several periodical structure. As the effective optical axis is still rotating, the birefringence of the DHFLC changes seriously and the ellipticity show up for the modulated light, like the conventional FLC electro-optical modes. The variation of the birefringence reduces the diffraction efficiency of the device, lower than the theoretically expected value. The phase retardation (δ)of the LC cell can be described by the function below[44],

$$\delta = \frac{2\pi\Delta nd}{\lambda}$$

1

here,Δn is the birefringence, d is the thickness or cell gap of the LC and λ is the wavelength. In the linear region, before the helix breaking point, the effective optical axis rotates in a limited range, corresponding to insufficient phase depth. This is also one of the reasons that most of the FLC can only achieve amplitude modulation and binary phase modulation[31]. The change of effective birefringence Δn in nonlinear region destroys the diffraction efficiency η and induces the change of polarization state, which is also contribute to the ellipticity modulation of the impinging light. Escuti's group has disclosed different kinds of achromatic waveplate and geometrical phase devices in the past few years by combining several waveplates with designed retardation and optical axis[45,46]. We designed a compensation film to compensate the birefringence change during the whole helix unwinding process of DHFLC to increase the phase modulation depth and reduce the ellipticity modulation issue.

As shown in Fig. 3, the proposed system based on DHFLC achieves continuous ~ 2π phase modulation at a voltage lower than 5 V (Electric field lower than 3.3 V/μm) in reflective mode. According to the measurement, the deviation of Δn and retardation reaches 50% from the half-wave condition (HW) before deformation (see red solid line in Fig. 3d). To compensate this variation, two retardation films were added with a fixed optical axis at the top and below of the DHFLC cell (shown in Fig. 3b), working as a fixed phase retarder to remain in the HW condition during the whole unwinding process. The compensation films to maintain the half-wave condition during helix unwinding. According to the geometrical phase theory, when the retardation of the anisotropic material is in HW condition, the output light contains the phase information related to the direction of the optical axis α, which is the function of E.

$$M_{DHFLC} = \begin{bmatrix} cos\alpha & sin\alpha \\ -sin\alpha & cos\alpha \end{bmatrix} \begin{bmatrix} e^{-i\frac{\pi\Delta nd}{\lambda}} & 0 \\ 0 & e^{i\frac{\pi\Delta nd}{\lambda}} \end{bmatrix} \begin{bmatrix} cos\alpha & -sin\alpha \\ sin\alpha & cos\alpha \end{bmatrix};$$

2

$$M_{QWP} = \begin{bmatrix} e^{-i\frac{\pi}{4}} & 0 \\ 0 & e^{i\frac{\pi}{4}} \end{bmatrix}$$

3

$$E_{out} = M_{DHFLC} * M_{QWP} * M_{QWP} * M_{DHFLC} * \frac{1}{\sqrt{2}} \begin{bmatrix} 1 \\ i \end{bmatrix} = e^{-i4\alpha} * \frac{1}{\sqrt{2}} \begin{bmatrix} 1 \\ -i \end{bmatrix}$$

4

In the given device structure, the phase depth is 4 times of the rotation range of the optical axis of the DHFLC, which is 8 times of the tilt angle of the DHFLC. With the compensation film, we found that the experimental results are matching well with the theoretical predictions in both transmissive mode and reflective mode. The optimization on the tilt angle of the DHFLC with host and chiral dopant combination for the nano helix-pitch DHFLC, extend the whole blue map of ferroelectric unit based phase modulations. The details about the materials compared and optimized in the paper are shown in Supplementary Materials 2.1–2.3 and Extended Data Figs. 3 and 4. The simulation of FFE with different material parameters are also analysed, the details are shown in Extended Data Figs. 6 and 7. The maximum tilt angle we have achieved is 42.5°, corresponding to phase depth by 1.9π with response time < 250 μs for a sufficiently wide temperature range(Table 2).

For the device demonstration of high spatial resolution applications, firstly, for the 1D or 2D blazed grating profile, the passively addressed matrix SLM. based on DHFLC is designed with a 3 μm pixel size (see Fig. 4.a and b). Specifically, various voltages (0 − 7 V) with different voltage steps are applied to each pixel to achieve the greyscale map. The intensity on the electrodes are different where electric fields with inverse polarity are applied, which showcases the DHFLC's phase modulation ability. The continuous multiple grey scale can be achieved by controlling the voltage. Along that an FLC polarization-dependent blazed grating is fabricated to verify the possibility of the applications for beam-steering and tunable polarization beam splitter. The electrode spacing is fixed at 2 μm, due to limitations on the fabrication facilities. We achieved the maximum diffraction efficiency of 77% (see in. Figure 4d). The detailed performance and measurement results of the demonstration are shown in Extended Data Fig. 8. Finally, the proposed DHFLC SLM shows defect-free, fast (~ 100 μs) phase modulation, which can find application in range of photonics.

Discussion

According to the obtained results of the unwinding process, the birefringence is almost unchanged in the linear range when $E \ll Ec$. The constant birefringence and effective optical axis rotation can show tunable geometrical phase modulation. However, in the broken helix region, when $E \gg Ec$, the effective birefringence increases and the phase modulation inters into the non-linear regime. The optical axis rotation and helix unwinding of the DHFLC strongly depends on the balance between the elastic torque, spontaneous torque and the dielectric displacement torque. We studied the linear region and non-linear region for the phase modulation (Fig. 3d). As the first example, we used the DHFLC with helix-pitch of ~ 120 nm, where the periodical structure cannot be observed since the light wavelength is much larger than the helix-pitch, and the effective birefringence behaves as a uniaxial retarder. Though, the helix starts to deform in the presence of the electric field, as shown in Fig. 1d, it is still far smaller than the wavelength of the impinging light. When the light passes through the DHFLC, DHFLC works as a waveplate with the optical axis rotating, only if $p < \lambda$ during the deformation. Since the direction of P_s is perpendicular to the molecular during rotation, the effective optical axis will rotate (in XY-plane) to either positive or negative polarity with an angle (α) when $-E$ or E are applied. It is worth mentioning here that maximum α depends on the cone angle (2θ) of FLC molecular. If θ= 45°, that is to say, rotation 2θ= 90° when positive and negative electric field applied, then the half-wave condition can be achieved just by adjusting cell gap (d) and Δn. Under this condition, fast π (transmissive mode) and 2π (reflected mode) phase modulation can be achieved within a small voltage range when the d and Δn match the HW conditions.

According to the schematic diagram in Fig. 1d, where the DHFLC is planar aligned along the alignment direction (Z-axis). The electric field direction is perpendicular to the substrates. The effective projection of the P_s on the plane of the SmC layer is the P_s of single FLC molecule shown in the schematic graph Fig. 1c. When the electric field is applied along the Z-direction, theP_s vector tries to follow the electric field, and thus, the FLC molecules rotate in-plane simultaneously. Thus, for the DHFLC to work in the linear reason the designed FLC must possess large E_c, which is primarily dictated by the spontaneous polarization and the elastic energy of the FLC material. The E_c is related toP_s and helical pitch (p) as below.

$$E_c = \frac{\pi^2 K \left(\frac{2\pi}{p}\right)^2}{16 P_s}$$

5

Here, K is the twist elastic constant of the FLC[48,49]. Hence by optimizing P_s, K and p, we were able to increase the E_c and the linear modulation region of the DHFLCs.

In a nutshell, 3 key achievements are shown in this article as follows. First, high-contrast defect-free DHFLC is utilized for phase modulation after optimization in the alignment quality.. The proposed no-FFE can achieve pixel size below 1 μm for monochromatic photonic devices with fast response. Innovatively, it is the first time that continuous phase modulation with 2π phase depth and fast switching time (250 μs

at 500 Hz), working at low voltage (< 5 V) with high efficiency (> 90%) are achieved based on the geometrical phase modulation of DHFLC. The proposed design is a promising candidate for various technologies, such as high-pixel-density imaging, WSS, adaptive optics, and optical communication, so forth. Second, the maintained polarization is achieved with the compensation film design, which drops the DHFLC material deviation from 20% to < 0.1%, that solves the long-term problem of ellipticity modulation. Finally, by optimizing the DHFLC material we achieved 1.9π phase modulation range and ~ 100 μs response time with low voltage (5 V) driving scheme. A circularly polarization-dependent blazed grating with 77% diffraction efficiency without FFE. are fabricated, which shows great potential for large deflection angle, high-efficiency beam steering, high bandwidth WSS, hologram, and adaptive optics when driven by active matrix or Si backplane.

Declarations

Acknowledgements

This research is supported by The State Key Laboratory of Advanced Displays and Optoelectronics and ITF. grant number P.R.P./049/19FX, through the Innovations and Technology Commission of Hong Kong

Author Contributions

Z.S., and Z.Y. conceived and simulated the research idea. Z.S. performed the electro-optical experiment and analysed the data. Z.Y. helped with the fabrication of samples and implementation of experiment setup. V.S. conceived the idea of studying the helix unwinding process and the respective cell design; Z.S., A.C. and L.L. designed the driving of the device. Z.S. wrote the manuscript with assistance from all the authors. V.V. and E.V. designed, synthesised and composed the Ferroelectric Liquid Crystals. H.S. and A.K.S. supervised the research.-

Corresponding author:

Correspondence to Abhishek K Srivastava

Conflict of Interest Statement

There is no conflict of interest.

References

1. Cao, Z. *et al.* Reconfigurable beam system for non-line-of-sight free-space optical communication. *Light Sci. Appl.***8**, 1-9 (2019).
2. Smolyaninov, A., El Amili, A., Vallini, F., Pappert, S. & Fainman, Y. Programmable plasmonic phase modulation of free-space wavefronts at gigahertz rates. *Nat. Photonics***13**, 431-435 (2019).

3. Li, J., Yu, P., Zhang, S. & Liu, N. Electrically-controlled digital metasurface device for light projection displays. *Nat Commun***11**, 3574 (2020). https://doi.org:10.1038/s41467-020-17390-3
4. Guo, X., Ding, Y., Duan, Y. & Ni, X. Nonreciprocal metasurface with space–time phase modulation. *Light Sci. Appl.***8**, 1-9 (2019).
5. Yuan, Z.-N., Sun, Z.-B., Kwok, H.-S. & Srivastava, A. K. Fast LiDAR systems based on ferroelectric liquid crystal Dammann grating. *Liq. Cryst.*, 1-15 (2021).
6. Jiang, Y., Karpf, S. & Jalali, B. Time-stretch LiDAR as a spectrally scanned time-of-flight ranging camera. *Nat. Photonics***14**, 14-18 (2019). https://doi.org:10.1038/s41566-019-0548-6
7. Park, J., Won, K. & Kim, Y. Liquid crystal between two distributed Bragg reflectors enables multispectral small-pitch spatial light modulator. *Light Sci. Appl.***11**, 210 (2022). https://doi.org:10.1038/s41377-022-00882-w
8. Yuan, Z.-N. *et al.* in *SID Symp. Dig. Tech. Pap.* 439-442 (Wiley Online Library).
9. Srivastava, A. K., de la Tocnaye, J. d. B. & Dupont, L. Liquid crystal active glasses for 3D cinema. *J. Disp. Technol.***6**, 522-530 (2010).
10. Srivastava, A., Hu, W., Chigrinov, V., Kiselev, A. & Lu, Y.-Q. Fast Ferroelectric liquid crystal grating based on orthogonal photo alignments. *Appl. Phys. Lett***100**, 1-031112 (2012).
11. Hampson, K. M. *et al.* Adaptive optics for high-resolution imaging. *Nat. Rev. Methods Primers***1**, 68 (2021). https://doi.org:10.1038/s43586-021-00066-7
12. Booth, M. J. Adaptive optical microscopy: the ongoing quest for a perfect image. *Light Sci. Appl.***3**, e165-e165 (2014). https://doi.org:10.1038/lsa.2014.46
13. Qin, Z. *et al.* Adaptive optics two-photon microscopy enables near-diffraction-limited and functional retinal imaging in vivo. *Light Sci. Appl.***9**, 79 (2020). https://doi.org:10.1038/s41377-020-0317-9
14. Xi, P., Wei, X., Qu, J. & Tuchin, V. V. Shedding light on biology and healthcare—preface to the special issue on Biomedical Optics. *Light Sci. Appl.***11**, 156 (2022). https://doi.org:10.1038/s41377-022-00804-w
15. Bakas, S., Uttamchandani, D., Toshiyoshi, H. & Bauer, R. MEMS enabled miniaturized light-sheet microscopy with all optical control. *Sci. Rep.***11**, 14100 (2021). https://doi.org:10.1038/s41598-021-93454-8
16. Matsuyama, S. *et al.* Nearly diffraction-limited X-ray focusing with variable-numerical-aperture focusing optical system based on four deformable mirrors. *Sci. Rep.***6**, 24801 (2016). https://doi.org:10.1038/srep24801
17. Bani Hassan, N. *et al.* Ultrahigh frame rate digital light projector using chip-scale LED-on-CMOS technology. *Photonics Res.***10**, 2434 (2022). https://doi.org:10.1364/prj.455574
18. Sanders, S. N. *et al.* Triplet fusion upconversion nanocapsules for volumetric 3D printing. *Nature***604**, 474-478 (2022). https://doi.org:10.1038/s41586-022-04485-8
19. Qin, Z. *et al.* Deep tissue multi-photon imaging using adaptive optics with direct focus sensing and shaping. *Nat. Biotechnol.* (2022). https://doi.org:10.1038/s41587-022-01343-w

20. Lingel, C., Haist, T. & Osten, W. Optimizing the diffraction efficiency of SLM-based holography with respect to the fringing field effect. *Appl. Opt.***52**, 6877-6883 (2013).
21. Wang, X. *et al.* Fast and low loss flexoelectro-optic liquid crystal phase modulator with a chiral nematic reflector. *Sci. Rep.***9**, 7016 (2019). https://doi.org:10.1038/s41598-019-42831-5
22. Hwang, C.-S. *et al.* in *SID Symp. Dig. Tech. Pap.* 297-300 (Wiley Online Library).
23. Tao, X., Norton, A., Kissel, M., Azucena, O. & Kubby, J. Adaptive optical two-photon microscopy using autofluorescent guide stars. *Opt. Lett.***38**, 5075-5078 (2013).
24. Aviles-Espinosa, R. *et al.* Measurement and correction of in vivo sample aberrations employing a nonlinear guide-star in two-photon excited fluorescence microscopy. *Biomed. Opt. Express***2**, 3135-3149 (2011).
25. Cha, J. W., Ballesta, J. & So, P. T. Shack-Hartmann wavefront-sensor-based adaptive optics system for multiphoton microscopy. *J Biomed Opt***15**, 046022 (2010). https://doi.org:10.1117/1.3475954
26. Li, P., Wang, X.-Q., Shen, D. & Zheng, Z.-g. A long-term stable low-viscous self-organized blue phase liquid crystal superstructure with wide operation temperature range. *Liq. Cryst.***49**, 192-200 (2022).
27. Zhao, R. *et al.* Effect of the introduction of mono-functional monomer on the electro-optic properties of reverse-mode polymer stabilised cholesteric liquid crystal. *Liq. Cryst.***48**, 1162-1174 (2021).
28. *BOE Technology Group Co., Ltd.*, <https://boe.com/> (
29. Clark, N. A. & Lagerwall, S. T. Submicrosecond bistable electro-optic switching in liquid crystals. *Appl. Phys. Lett.***36**, 899-901 (1980).
30. Love, G. D. & Bhandari, R. Optical properties of a QHQ ferroelectric liquid crystal phase modulator. *Opt. Commun.***110**, 475-478 (1994). https://doi.org:https://doi.org/10.1016/0030-4018(94)90234-8
31. Nabadda, E. *et al.* Ferroelectric liquid-crystal modulator with large switching rotation angle for polarization-independent binary phase modulation. *Opt. Lasers Eng.***159**, 107204 (2022).
32. Kotova, S. P., Samagin, S. A., Pozhidaev, E. P. & Kiselev, A. D. Light modulation in planar aligned short-pitch deformed-helix ferroelectric liquid crystals. *Phys. Rev. E***92** (2015). https://doi.org:10.1103/physreve.92.062502
33. Kotova, S. P. *et al.* Ferroelectric liquid crystal with sub-wavelength helix pitch as an electro-optical medium for high-speed phase spatial light modulators. *Opt. Laser Technol.***135**, 106711 (2021).
34. Sun, Z., Yuan, Z., Shi, R., Kwok, H.-S. & Srivastava, A. K. Fringe field effect free high-resolution display and photonic devices using deformed helix ferroelectric liquid crystal. *Liq. Cryst.***48**, 100-110 (2021).
35. Yuan, Z. N. *et al.* Microsecond high-contrast continuous 2.25 π phase modulation based on non-linear Kerr effect of vertically aligned deformed helix ferroelectric liquid crystal. *J. Soc. Inf. Disp.***30**, 404-412 (2022).
36. Beresnev, L. *et al.* Deformed helix ferroelectric liquid crystal display: a new electrooptic mode in ferroelectric chiral smectic C liquid crystals. *Liq. Cryst.***5**, 1171-1177 (1989).
37. Lazarev, G., Hermerschmidt, A., Krüger, S. & Osten, S. LCOS spatial light modulators: trends and applications. *Optical Imaging and Metrology: Advanced Technologies*, 1-29 (2012).

38. Fan-Chiang, K.-H., Wu, S.-T. & Chen, S.-H. Fringing-field effects on high-resolution liquid crystal microdisplays. *J. Disp. Technol.***1**, 304 (2005).
39. Chen, C.-H., Hsu, H.-F., Chen, H.-R. & Hsieh, W.-F. Non-interferometric phase retrieval using refractive index manipulation. *Sci. Rep.***7**, 1-8 (2017).
40. Zou, J. *et al.* Fast-Response Liquid Crystal for Spatial Light Modulator and LiDAR Applications. *Crystals***11**, 93 (2021). https://doi.org:10.3390/cryst11020093
41. Srivastava, A. K., Chigrinov, V. G. & Kwok, H. S. Ferroelectric liquid crystals: Excellent tool for modern displays and photonics. *J. Soc. Inf. Disp.***23**, 253-272 (2015).
42. Krivoshey, A. *et al.* p-Terphenyl-containing symmetric tetraesters for nano-scale pitch ferroelectric liquid crystal materials. *J. Mol. Liq.***356**, 119051 (2022).
43. Mikhailenko, V. *et al.* The nano-scale pitch ferroelectric liquid crystal materials for modern display and photonic application employing highly effective chiral components: Trifluoromethylalkyl diesters of p-terphenyldicarboxylic acid. *J. Mol. Liq.***281**, 186-195 (2019).
44. Guenther, B. D. *Modern optics*. (OUP Oxford, 2015).
45. Li, L. & Escuti, M. J. Super achromatic wide-angle quarter-wave plates using multi-twist retarders. *Opt. Express***29**, 7464-7478 (2021).
46. Sun, Z., Yuan, Z., Srivastava, A. K. & Kwok, H.-S. in *SID Symp. Dig. Tech. Pap.* 638-642 (Wiley Online Library).
47. Fowles, G. R. *Introduction to modern optics*. (Courier Corporation, 1989).
48. Dahl, I., Lagerwall, S. & Skarp, K. Simple model for the polarization reversal current in a ferroelectric liquid crystal. *Physical Review A***36**, 4380 (1987).
49. Lagerwall, S. T. Ferroelectric and antiferroelectric liquid crystals. *Ferroelectrics***301**, 15-45 (2004).
50. Lu, Q., Sheng, L., Zeng, F., Gao, S. & Qiao, Y. Improved method to fully compensate the spatial phase nonuniformity of LCoS devices with a Fizeau interferometer. *Appl Opt***55**, 7796-7802 (2016). https://doi.org:10.1364/AO.55.007796

Methods

Material preparation

Most of the material preparation is discussed in Material Design and Supplementary Materials 1.1-1.3.

Device fabrication

DHFLC works as a phase modulator. As for the fabrication shown in SI., the spin-coating process is chosen to deposit N_6 uniformly on the substrate with the patterned ITO, setting the speed to 3000 rpm for 2 min. After that, soft baking at 100 ℃ for 10 mins and hard baking at 180℃ for 1 hour to polymerize the N_6. Afterward, the substrate is rubbed unidirectionally. The cell is made using two substrates, where

the first substrate is patterned with ITO. and the other one is patterned with ITO. coated with a planarization layer (100 nm SiO_2). The cell gap is 2 μm by depositing photo-spacers uniformly. Finally, FLC material injection based on capillary action from one side to another side of the cell. The Nylon 6 (N_6), purchased from Merck & Co. Inc, is dissolved in 2,2,2 – Trichloroethhanol (0.5 wt %) and filtered through a 0.2 μm Teflon syringe filter in advance. The thickness of the Nylon 6 film is 30 nm on the substrate.

ITO pattern fabrication

As for the spatial light modulator with 3 pitch ITO pattern, a wet-etching process using Aqua Regia ($HCl:H_2O:HNO_3$ = 4:2:1) after photo-lithography (exposed by Karl Suss MA6 and HPR 504 as PR) is used to remove some of the ITO in the designed area. The 1 pitch is also fabricated. But due to the resolution limit which is much better in the industry, only 3 pitch shows no short circuit and can be controlled separately.

Simulation and Compensation film design

Due to the birefringence change during the unwinding process of the DHFLC, especially in the non-linear region, the birefringence and retardation of the DHFLC change rapidly by at least 0.04 and 20%, respectively. Such electro-induced dispersion (EID.) is the main bottleneck for most of the phase modulation process based on the helix unwinding or twist effect of LC With the conclusion given by the high elastic energy and observation in Fig. 2. The change of retardation under operating voltage for DHFLC is acceptably small which can be compensated by designed passive retardation film inspired by the broadband retardation film design proposed and optimized by Escuti's group[45]. After the simulation and optimization analysis based on the Jones Matrix and the proposed model of DHFLC in this work, a direct optimization with target function defined by the mismatch of the half-wave condition is done by sweeping the retardation, optical axis, and twist angle of the compensation film. The details of the optimization are in Supplementary Materials 2.4 and Extended Data Figure 5.

$$target\ function = min(R(\beta) * M_{film2} * R(-\beta) * R(\alpha) * M_{DHFLC} * R(-\alpha) * R(\gamma) * M_{film1} * R(-\gamma)) \quad (6)$$

Here the α, β and γ are the optical axis of the DHFLC, output compensation film and input compensation film, respectively. The α is tunable under different electric fields. However, the compensation method for the EID. is proposed firstly to work out the ellipticity change in the high PPI phase modulation using DHFLC. As a result, the director and retardation of the designed compensation film are and (β =14.54°,δ=1.81;γ =-14.54°,δ=1.81) for 2π phase modulation range at 632 nm when the cell gap of the DHFLC is 1.67 μm, respectively. Here δ is the retardation of the compensation film.

Measurement

The phase modulation range is measured in two modes, one is transmissive mode utilizing Michelson interferometer, and the other one is reflective mode utilizing Mach-Zehnder interferometer[50]. In the transmissive mode, uniform aligned incident light (diameter = 1 cm) is expanded and filtered before the beam splitter. The light is separated into 2 arms (one comparison arm without the DHFLC phase modulator and another one with the DHFLC phase modulator) with equal intensity. The phase difference would be detected by the detector from the interference of these 2 light paths. Specifically, when the light passes through the DHFLC with uniaxial compensation film, the polarization state is converted into orthogonal circularly polarized light. Moreover, the optical axis deflection induced phase change which is controlled by the applied voltage to the DHFLC. After the two light arms encounter at the second BS, then the interference intensity of the light is measured by the detector. In the reflected mode, the light is first converted into circularly polarized light through a quarter wave plate after the beam is expanded and filtered. Then it is divided into two circularly polarized beams with the same intensity after passing through the BS For the comparison light arm, the light reflects and passes through a quarter-wave plate again, converting the light orthogonal to the input light. For the other arm with DHFLC cell, the light converts into circularly polarized light which is orthogonal to the initial incident state. When the electric field is applied to the DHFLC, the light transfers into circularly polarized light with electric-field-dependent phase variance. After that, the reflection elements units (quarter-wave plate (QWP. 1) and mirror) tune the polarization state into orthogonally circular polarized light, which is the same as the polarization state on the comparison arm. Finally, the 2 light beams interface at the BS before the detector and then the phase difference could be derived from the recorded interference light intensity. Compared with the transmissive mode, due to the QWP. between the DHFLC and mirror, the polarization state changes at a second time after the reflection, double the phase, making the total phase modulation range of the DHFLC twice larger than the phase depth in transmissive mode.

Tables

Table 1 is available in the Supplementary Files section

Table 2 Composition and Basic Characteristics of DHFLC Materials based on BPP-73 Host Used in Current Work. (Data are taken at 25°C)

Code	Chiral Component	c, mol %	Phase transitions[1], °C	*p*, nm	*H.T.P.*, μm^{-1}	*q*, °	P_S, nC/cm^2	*Vc*, Volt
587	FODTA-6[2]	24.0	Iso 115.5 SmA 97.5 SmC* 9.5 Cr	118[3]	36[3]	37.5	150	7
9074	FODTA-6	25.1	Iso 107.6 SmA 94.2 SmC* 1.9 Cr	110[4]	36.3[4]	36.5	105	10
9075	DFT-TFA-6	25.1	Iso 113.2 SmA 95.1 SmC* 5.2 Cr	95[4]	42.1[4]	39	138	8
9146	PDN-TFA-6	16.8	Iso 123.2 SmA 98.9 SmC* 14.0 Cr	123	48.4	41.5	100	9
11066	PDN-TFA-6	25.0	Iso 106.6 SmA 99.8 SmC* 12.0 Cr	99[4]	40.4[4]	42.5	164	7

[1] All phase transition measured using DSC in cooling mode at 2 °/min, except melting point measured in heating mode at 1°/min

[2] BPP-6587 host was used

[3] Data taken from Ref[43]. If any, we can use for these materials EOP. data measured here

[4] Extrapolated value, see Supplementary Materials 1.1-1.3. for details

Figures

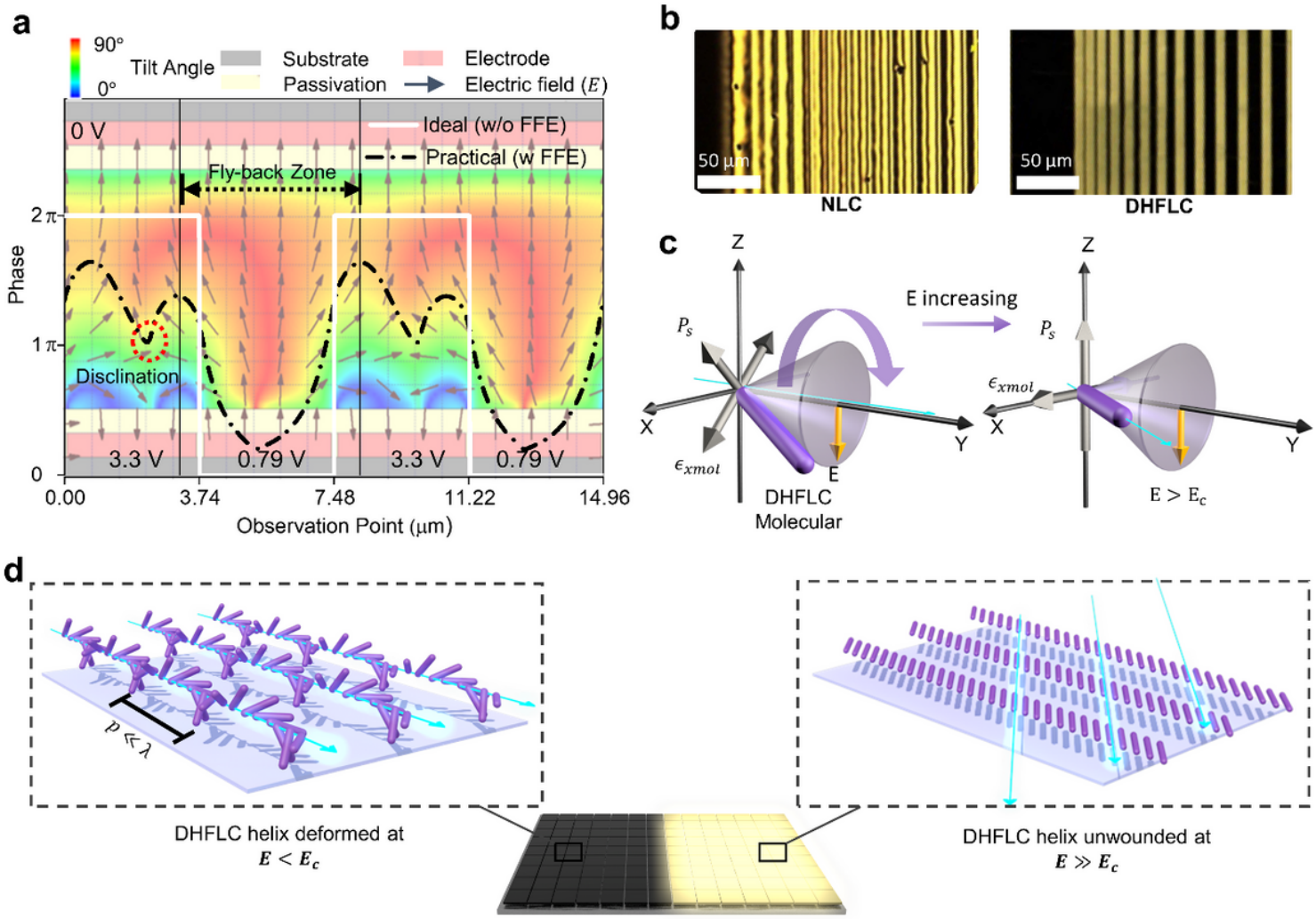

Figure 1

Concept of FFE. and the deformed helix ferroelectric dynamic rotation. a The phase profile for FFE. analysis, without (labelled in white solid line) and with (labeled in black solid line) FFE. for 2 pixels (“on” and “off”) in 1 period. The pixel size and inter-gap between the pixels are 3.74 μm and 0.2 μm, respectively. The sub-image is the tilt angle, and electric field distribution under the simulation with FFE. b The polarization optical microscopic picture (POM. ×20) for alignment quality and FFE. comparison of NLC (left) and FLC (right) under incremental electrode gap from 1 μm to 50 μm. c The schematic for single molecular rotation along the rotation cone with electric field increasing gradually larger than critical unwinding voltage (E_c), ε_x is the dielectric constant along X-axis. d The schematic of planar-aligned DHFLC molecular configuration without (left) and with (right) electric field applied in the vertical direction (Z-axis).

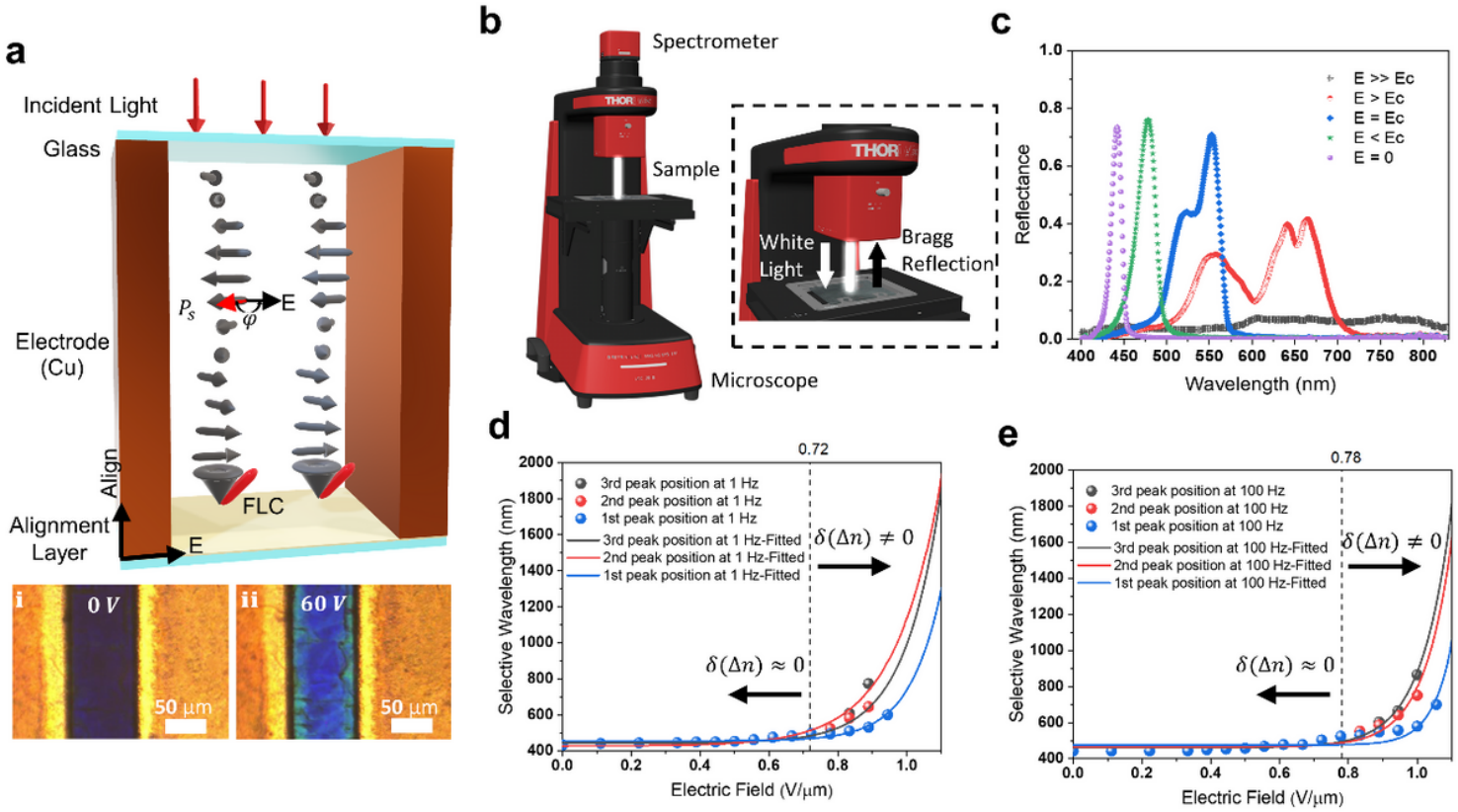

Figure 2

The schematic and experimental results for the unwinding process study and dynamic model construction. a The schematic of the test cell structure for unwinding process observation. The sub-figures below are the POM. (left) of no electric field applied between Cu electrodes and the POM. (right) of E= 0.8 V/μm applied between Cu electrodes. The helix of the FLC in the measurement area (10 μm*10 μm in the middle) is aligned vertically and parallel to electrode. b The measurement setup of the reflective spectrum. White light is incident normally from the top. c Reflective spectrum versus wavelength at different applied electric fields. The selective wavelength (derived from the corresponding wavelength where the reflectance peak exists) *vs*applied voltage at d 1 Hz and e 100 Hz. The dashed line separates the linear modulation region with deformed helix (without birefringence change) and the non-linear region with broken helix (with birefringence change).

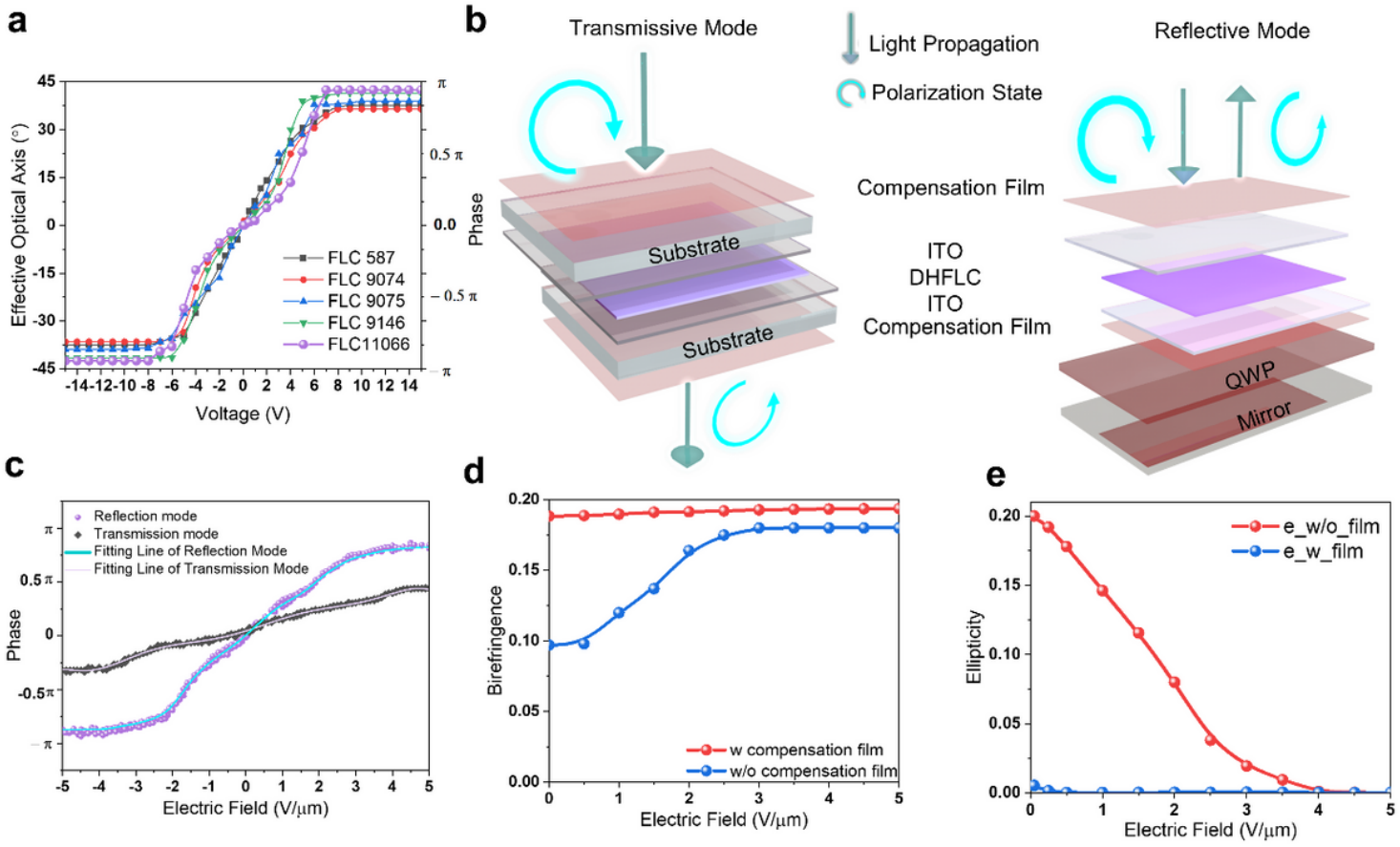

Figure 3

Schematic and experiment results of retardation compensation. a Phase versus electric field in transmissive mode and reflective mode. The measurement setup is in (Extended Data Figure 3). bSchematic of a device structure with compensation film in transmissive mode (left) and reflective mode (right). c the measurement of different DHFLC in Table 2. The direction of the effective optical axis corresponds to the phase given by the geometrical phase. dMeasurement results of effective birefringence versus electric field for DHFLC 587 at 632 nm: with(w) and without (w/o) compensation film. e The comparison of measured ellipticity between the device with (red dot line) and without (black dot line) compensation films in the experiment. Ellipticity is measured and calculated by the polarization ratio of the output polarization state when a linear polarized light is incident light. Details are in Supplementary Materials 2.4 and Extended Data Figure 5.

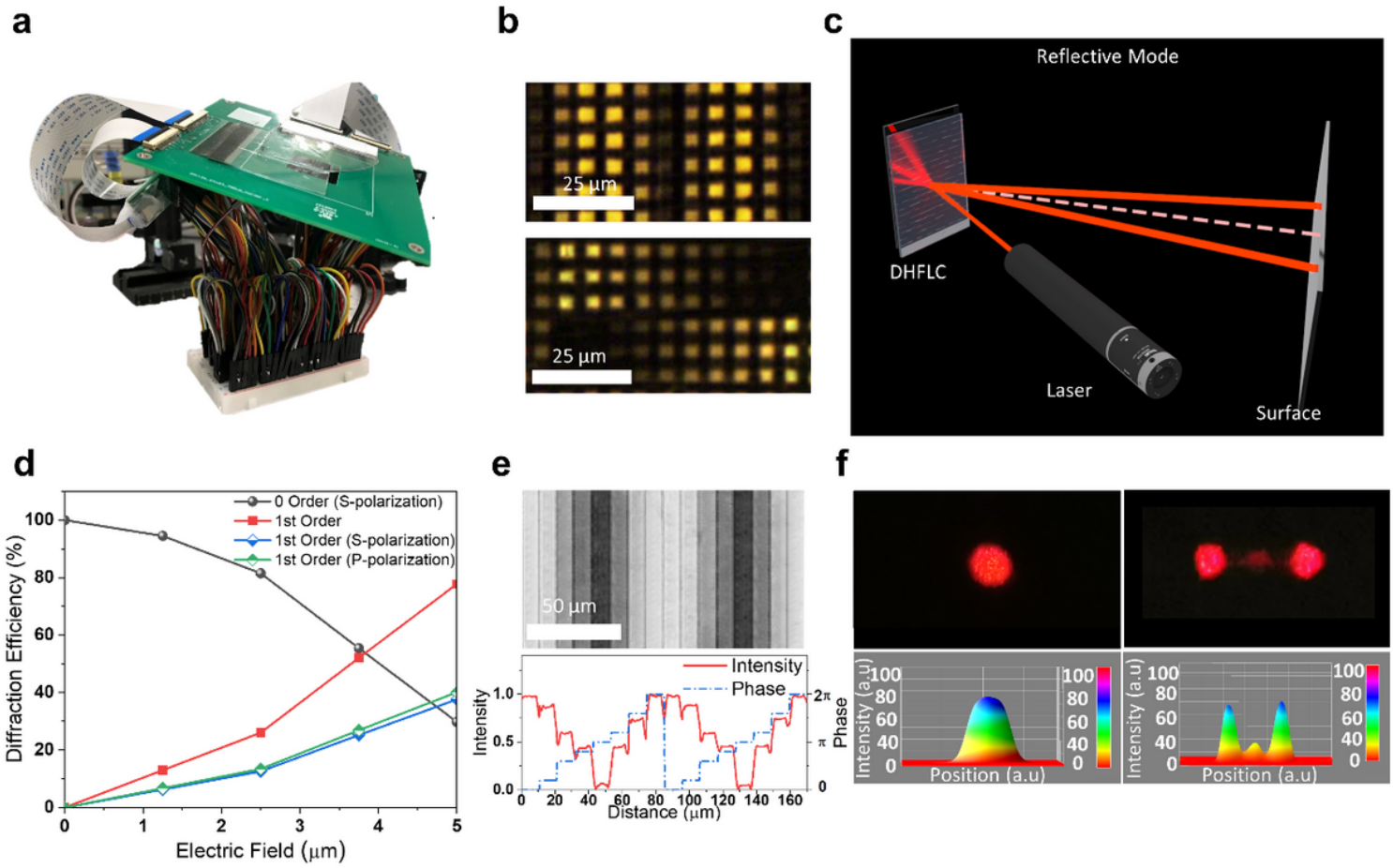

Figure 4

Experimental results for 1D 2D blazed grating and 2D beam steering. a The picture of the passively addressed prototype with 3 μm pixel size. b The POM. of a. and DHFLC on passive driving matrix with 3 μm pixel size. c. the measurement setup of the diffraction profile and diffraction efficiency. d The diffraction efficiency of the polarization-dependent blazed grating in (e). e POM. of the polarization-dependent blazed grating configuration with electrode pattern and inter-resist connection. The image below is the intensity profile and phase profile. f The non-diffraction image and corresponding intensity map (left). The diffraction image and corresponding intensity map (right).

Supplementary Files

This is a list of supplementary files associated with this preprint. Click to download.

- LSAExtendedDatawithlegendSubmission.docx
- LSASupplementaryMaterialssubmission.docx
- Table1.docx